



# Sintering Characteristics of Thermal Barrier YSZ Coatings Made by Suspension Plasma Spraying

M. Giżyński<sup>1,2,3</sup> · X. Chen<sup>1,4</sup> · H. Araki<sup>1</sup> · H. Tanaka<sup>1</sup> · S. Kuroda<sup>1</sup> · M. Watanabe<sup>1</sup> · Z. Pakieła<sup>2</sup>

Submitted: 25 August 2021 / in revised form: 9 January 2022 / Accepted: 11 January 2022 / Published online: 22 March 2022  
© ASM International 2022

**Abstract** Thermal barrier coatings (TBCs) deposited by suspension plasma spraying (SPS) are recognized as a potent method to increase efficiency and extend the life of gas turbines. The unique microstructure of the SPS coatings provides exceptional mechanical and thermal properties, but on the other hand, affects sintering of the TBCs what could lead to undesirable changes in properties and premature failure. This study attempts to characterize changes occurring in the SPS deposited TBCs during high-temperature exposure. Several SPS yttria-stabilized zirconia coatings were deposited with various spraying parameters including plasma gas composition, standoff distance and suspension. Then, the SPS coatings were subjected to temperature of 1150°C. It turned out that sintering shrinkage of SPS coatings was higher by a factor of 2-4 than APS coating. Detailed analysis of microstructural changes showed that the coatings with limited porosity at high temperature tend to form arrays of fine pores, while the coatings with higher initial porosity formed large spherical pores. Most of the SPS coatings showed a non-typical change of mechanical properties—a decrease in the Young's modulus and toughness. It was shown that

peculiar evolution of mechanical properties can be associated with the porosity changes and interactions between pores and propagation crack.

**Keywords** dilatometer · plasma spraying · sintering · thermal barrier coatings (TBC) · yttria-stabilized zirconia polycrystal

## Introduction

Ceramic thermal barrier coatings (TBCs) are widely used in hot sections of land-based gas turbines and aero-engines to increase the efficiency and extend the life of metallic components (Ref 1-3). The primary function of the TBC system is to provide a low-thermal-conductivity barrier, allowing to keep the temperature of metallic components moderate while increasing gas operating temperature. The advanced land-based turbine could operate at a temperature as high as 1600°C; the TBC together with internal cooling enable to reduce the temperature of the turbine component, e.g., blade or vane, by 150-200°C. 6 - 8 wt.% yttria-stabilized zirconia (YSZ) is still the state-of-the-art material for TBC application due to its favorable thermomechanical properties, i.e., low thermal conductivity, high coefficient of thermal expansion and high toughness. Nowadays, YSZ-based TBCs are fabricated by either plasma spraying (PS) or electron beam physical vapor deposition (EB-PVD). The application of each method results in dissimilar and distinctive coatings. The PS coatings consist of lamellae of numerous splats and have low thermal conductivity due to a myriad of intersplat voids and microcracks. The typical EB-PVD coatings, on the other hand, show columnar microstructure and exhibit low stiffness and high strain tolerance (Ref 4-7).

✉ M. Giżyński  
maciej.gizynski@ilot.lukasiewicz.gov.pl

<sup>1</sup> National Institute for Materials Science (NIMS), 1-2-1 Sengen, Tsukuba, Ibaraki 305-0047, Japan  
<sup>2</sup> Faculty of Materials Science and Engineering, Warsaw University of Technology (WUT), Wołoska 141, 02-507 Warsaw, Poland  
<sup>3</sup> Research Network Łukasiewicz-Institute of Aviation, al. Krakowska 110/114, 02-256 Warsaw, Poland  
<sup>4</sup> Jinan University, Tianhe District, No.601 West Huangpu Avenue, Guangzhou 510632, People's Republic of China

The YSZ-based TBC technology has been developed since the 80s, but to meet more demanding requirements, new directions of research have been taken. Recent studies have focused on two main fields, one of which is the development of new ceramic materials with increased maximum operating temperature, reduced thermal conductivity and sintering rate. Examples of such materials are  $Gd_2Zr_2O_7$  or ceramics with perovskite structure like  $SrZrO_3$  and  $BaZrO_3$  (Ref 8). The other research direction is the development of new deposition methods, such as plasma spray physical vapor deposition (PS-PVD) (Ref 9), solution precursor plasma spray (SPPS) (Ref 10–11) and suspension plasma spray (SPS) (Ref 12–14). Recently, the SPS method has attracted much attention because it allows for the multi-scale design of the TBC microstructure. Sub-micrometer or nanoparticles suspended in ethanol or water used as feedstock give a chance of realizing fine microstructures with sub-micrometer splats and nanoporosity. These attributes of the microstructure are expected to greatly reduce thermal conductivity. Previous studies have demonstrated that various coating structures can be realized by the SPS process, including vertically cracked and columnar microstructure (Ref 15–16), which may result in significant improvement in the durability and lifespan of YSZ TBC.

Sintering of YSZ TBC has been recognized as one of the major degradation processes resulting in final failure. Sintering of TBC materials at high temperature is disadvantageous, because it increases thermal conductivity and stiffness (Ref 17–21) and reduces thermal shock resistance (Ref 22). As serious efforts have been made to increase turbine efficiency by increasing the operating temperature, the sintering of TBC ceramic top coat has become an even more important issue. The finer microstructure of SPS TBCs top coat may accelerate sintering, microstructure changes and evolution of properties during high-temperature exposure. The well-established models of ceramics or plasma-sprayed TBCs sintering predict that the smaller the size of the splats in the ceramic coating is, the faster the sintering process proceeds (Ref 23–24). Nevertheless, detailed void analysis carried out by Bacciochini et al. (Ref 25) using ultra-small-angle X-ray scattering showing the presence of fine pores with a size of tens of nanometers after 100h of heat treatment at 1100°C or decrease in the hardness and Young's modulus reported after 100h of heat treatment at 1200°C and 1400°C by Chen et al. (Ref 26) indicates that sintering and sintering-related phenomena in SPS coatings are not so straightforward and need further investigation.

The objective of this study is to investigate the thermomechanical properties of various SPS coatings such as

the coefficient of thermal expansion and sintering shrinkage rate and to find a correlation between coating microstructure and sintering. The SPS coatings were deposited with various spraying conditions and with two suspensions, i.e., ethanol- and water-based. Detached coatings were heated to 1150°C, while the length changes during heating and isothermal heat treatment were recorded. Detailed microscopic studies before and after thermal heat treatment were carried out to shed light on the evolution of the coating microstructure. The change of mechanical properties was evaluated by a hardness test. Obtained results for SPS coatings were compared with those of a conventional TBC deposited by atmospheric plasma spraying.

## Experiment

### Materials and Spraying Procedure

Two suspensions of YSZ (8 wt.% yttria-stabilized zirconia) were used in this study. The first one was ethanol-based suspension with the powder loading of 25 wt.%. For the suspension preparation, commercially available fused and crushed powder (YSZ, Imerys Fused Minerals, Laufenburg, Germany) with a  $D_{50}$  of 0.42  $\mu\text{m}$  (Fig. 1a) and reagent grade ethanol (99.5%) as the solvent were mixed, followed by ball milling for 24 h by using  $ZrO_2$  balls and polyethylenimine as a dispersant. The second suspension was water-based suspension prepared by H.C. Stark GmbH, of which solid content was 30 wt. % and  $D_{50}$  of YSZ powder was 0.9  $\mu\text{m}$ .

The SPS process was carried out by an Oerlikon Metco Multicoat plasma spray unit with a Triplex Pro 210 gun. The plasma torch nozzle diameter was fixed at 9 mm. Suspension in a reservoir was pressurized by argon and radially injected to the plasma jet through an orifice with a diameter of 200  $\mu\text{m}$ . Detailed parameters of the SPS process are listed in Table 1. Two plasma gas compositions and two standoff distances were chosen to find the effect of the spraying parameters on the microstructure and thermomechanical properties of the coating. For the S1 and S2 coatings, the plasma jet was generated by an argon–helium mixture operated at a power of 44 kW. For the S3 and S4 coatings, an argon–hydrogen plasma was used, which should provide a higher thermal conductivity of plasma and enhance heat transfer from plasma to the used suspension. When the argon–hydrogen plasma was used, the power level rose to 58 kW. We used the conventional YSZ coating (A1) deposited by APS as a benchmark in this study. The feedstock material in this experiment was

**Fig. 1** Morphology of YSZ powder particles left after evaporation of the ethanol from ready-to-spray suspension (a). Morphology of Sulzer Metco 204NS used as feedstock in APS deposition (b)

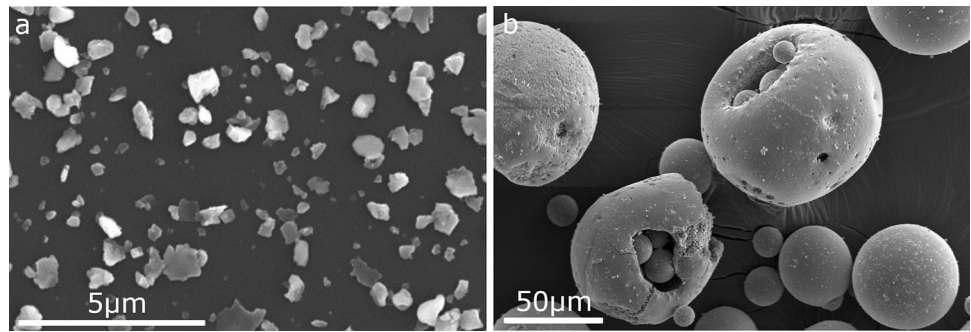


**Table 1** APS and SPS parameters for YSZ coating deposition

Coating	Method	Feedstock	Suspension feed rate	Standoff	Plasma composition	Output Power
A1	APS	204NS powder	.	100 mm	Ar/He	26 kW
S1	SPS	Ethanol-based suspension	32	50 mm	Ar/He	44.2 kW
S2	SPS	Ethanol-based suspension	32	70 mm	Ar/He	44.2 kW
S3	SPS	Ethanol-based suspension	25	50 mm	Ar/H <sub>2</sub>	53.4 kW
S4	SPS	Water-based suspension	25	70 mm	Ar/H <sub>2</sub>	58.8 kW

commercially available Sulzer Metco 204NS hollow spherical oxide powder (HOSP) with particle size  $d_{50}$  of 40  $\mu\text{m}$  (Fig. 1 b). In the APS process, a Praxair SG-100 plasma gun was used. The target thickness of both APS and SPS coatings was around 400  $\mu\text{m}$ .

All coatings were deposited onto SUS304 stainless steel substrates with dimensions of 25 x 20 x 1.5 mm. Before spraying, substrates were grit-blasted by alumina and then degreased in acetone using ultrasonic for about 5 minutes. Before spraying, substrates were heated up to 200°C to improve adhesion. The torch transverse speed during the SPS process was 1000 mm/s, while during APS it was 200 mm/s.

In order to investigate the sintering process and changes of the coatings' microstructure and properties caused by high-temperature exposure, heat treatment was carried out in air for 10 and 50 hours.

### Material Characterization

Cross sections and fracture surfaces of the samples were examined by using a scanning electron microscopes (SEM; JEOL JSM-6010LA and Hitachi SU-8000 for high-magnification images). Coating porosity was evaluated by image analysis of the cross sections with 2500x and 5000x magnification using ImageJ 1.51j8 (National Institute of Health, USA) software. For each coating, at least 5 images were analyzed. For cross-sectional analysis, as-sprayed samples were cut with a SiC cutting wheel, mounted in epoxy resin and subjected to standard metallographic

preparation with final polishing with 0.2  $\mu\text{m}$  alumina suspension. The mechanical polishing could introduce defects into the microstructure and affect surface porosity, microcracks and other features of the microstructure; thus, it makes a careful investigation impossible. Therefore, the last stage of the sample preparation was ion milling by Hitachi IM4000. In ion milling technique, the beam of argon ions delicately removes a thin layer of deformed material revealing unchanged material. In the experiment, the ion beam accelerating voltage was 4 kV and the incident angle was set at shallow angles such as 85 or 88°. Fracture surfaces were obtained by bending the freestanding coatings before and after the dilatometry experiment. Prior to observation, the samples were coated with a thin Pt layer. The thin lamellas necessary for the TEM observations were cut out of the polished cross-sectioned specimens using a focus ion beam (FIB) technique. The Hitachi FB-2100 FIB apparatus was used to prepare suitable specimens. The device uses Ga ions accelerated by a voltage of 40 kV to mill the specimen. Before the milling, a protective layer of tungsten was deposited onto the region of interest. All specimens prepared by this method were cut perpendicularly to the coating's interface. The typical size of the thin lamella was 15 × 10  $\mu\text{m}$ , which allows observing details of the coatings such as column interiors and inter-columnar porosity. Specimens were observed using JEOL JEM-1200 EX TEM operating at an accelerating voltage of 120 kV. The observations were made in bright- and dark-field mode. The freestanding YSZ coatings samples before and after the dilatometric experiment were examined by

x-ray diffraction (XRD, Rigaku MiniFlex 600, Cu radiation,  $\lambda=1.5406 \text{ \AA}$ ) over  $2\theta$  values from  $20$  to  $120^\circ$  with a scanning rate of  $5^\circ/\text{min}$  by a step of  $0.02^\circ$  and for more detailed study over  $2\theta$  values of  $26\text{--}36^\circ$  and  $72\text{--}76^\circ$  with a scanning rate of  $1^\circ/\text{min}$  at a step of  $0.01^\circ$

### Dilatometry

For the dilatometry experiment, freestanding coating specimens were prepared. Smaller pieces with a dimension of  $7.8 \text{ mm} \times 10 \text{ mm} \times 1.5 \text{ mm}$  were cut out of the original coated substrate and were immersed in *aqua regia* until debonding. Dimensional changes were measured using a high-temperature dilatometer Netzsch 402E/7/E-PY. The dilatometer is equipped with an alumina setup, i.e., expansion probe and alumina sample holder, which allow working temperature ranging from RT to  $1700^\circ\text{C}$ . A heater made of graphite is located outside of a gastight protection tube and works in an argon atmosphere. Before the test, this experimental setup was calibrated with a sapphire rod-shaped sample. During the experiment, the specimens were heated in dry air with a heating rate of  $20^\circ\text{C}/\text{min}$  up to  $1150^\circ\text{C}$ , then held at  $1150^\circ\text{C}$  for 10 h and finally cooled down with a cooling rate of  $20^\circ\text{C}/\text{min}$  down to  $200^\circ\text{C}$ . Such a temperature profile allowed us to evaluate the CTE and sintering shrinkage of the specimens.

### Mechanical tests

Vickers microhardness measurements with a load of 300 g and dwell time of 15 s were taken on the polished cross sections of the freestanding coatings before and after exposure to high temperature. At least 12 measurements were taken for each sample. In this study, Vickers indents were generated with gradually increased forces to measure the toughness of the ceramic layers. Cracks resulting from the application of local force were observed on the indents' corners. The method relies on the determination of the critical load  $P_c$  required to initiate a crack with a critical size  $c_c$ . If the load is lower than  $P_c$ , no cracks are observed in the indent vicinity. A similar approach was employed by, e.g., Sniezewski et al. (Ref 27) and Lesage and Chicot (Ref 28). If the critical values  $P_c$  and  $c_c$  are known, the "Vickers indentation" toughness  $K_{VIF}$  can be calculated by following formula (Ref 29):

$$K_{VIF} = \alpha \frac{E^{1/2} P_c}{H^{1/2} c_c^{3/2}} \quad (\text{Eq 1})$$

where  $\alpha$  is constant ( $\alpha=0.016\pm 0.004$ ) (Ref 29), and  $E$  and  $H$  refer to Young's modulus and hardness of the tested material, respectively.

## Results

### Microstructure

The representative cross-sectional microstructures of the as-sprayed coatings are presented in Fig. 2. Typical for APS coatings lamellar microstructure was revealed in the coating A1 (Fig. 2a). Higher-magnification picture shows pores, microcracks and intersplat voids. Microstructures of the S1 coating are presented in Fig. 2(b). The S1 coating's microstructure exhibits a relatively dense coating with deep vertical cracks (it is labeled "A" in the image). Fig. 2(b) inset reveals very fine porosity in coating S1, and the largest pores are about  $1 \mu\text{m}$  in diameter. The microstructure of the S2 (Fig. 2c) coating is entirely different from the ones mentioned before. The coating is made up of columns separated by porous boundaries (B), and porosity bands (C) are visible inside individual columns. The zoom-in image reveals a wide size distribution of pores, resolidified and loosely bonded ceramic particles (D). Figure 2(d) reveals dense columnar microstructure of the S3 coating. Unlike the highly porous S2 coating, columns of the S3 coating are dense, and only some porosity bands (C) were found. A high-magnification image confirms dense microstructure and reveals horizontal voids between splats. The microstructure of the S4 coating is rather similar to the microstructure of the S1 coatings. Figure 4(e) shows dense coatings with deep vertical cracks (A), and the zoom-in image reveals that pores are coarser than in the S1 coating.

The high-temperature exposure did not change the *large-scale* (i.e., columnar or vertically cracked) structure of the coatings; however, it affected the *small-scale* elements of microstructure such as pores or microcracks. Figure 3 shows the small-scale microstructure evolution of the S1 and S2 coatings. These coatings were chosen for detailed examination due to their distinct sintering behavior, which was demonstrated by the dilatometric experiment. TEM images presented in Fig. 4 provide additional information about heat-induced changes of the S1 and S2 coatings. The microstructure evolutions of the S1, S3 and S4 coatings seem to be fairly similar, so only the S1 coating's microstructure is discussed here.

The as-sprayed microstructure of the S1 coating consisted of very fine splat with a thickness under  $1 \mu\text{m}$  and pores and intersplat voids with a diameter of a few  $\mu\text{m}$ . More detailed information is given by the TEM image presented in Fig 4(a). The micrograph shows two kinds of particles building the coatings—one is flat lamellas with a high aspect ratio, the thickness of a few hundred nm, usually around 200–300 nm (E). Single lamella consists of columnar grains of  $t/t'$ -ZrO<sub>2</sub>, the height of columnar grains

**Fig. 2** Cross section of as-sprayed coatings A1 (a), S1 (b), S2 (c), S3 (d) and S4 (e)

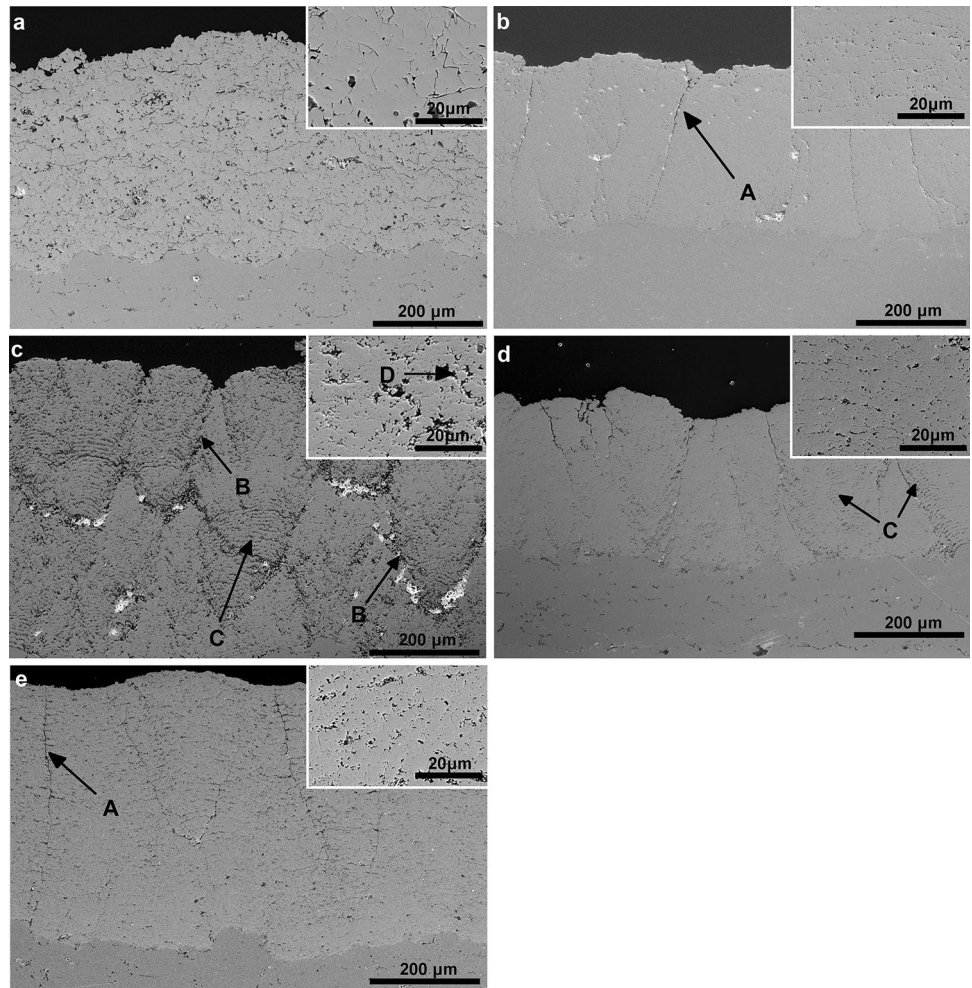
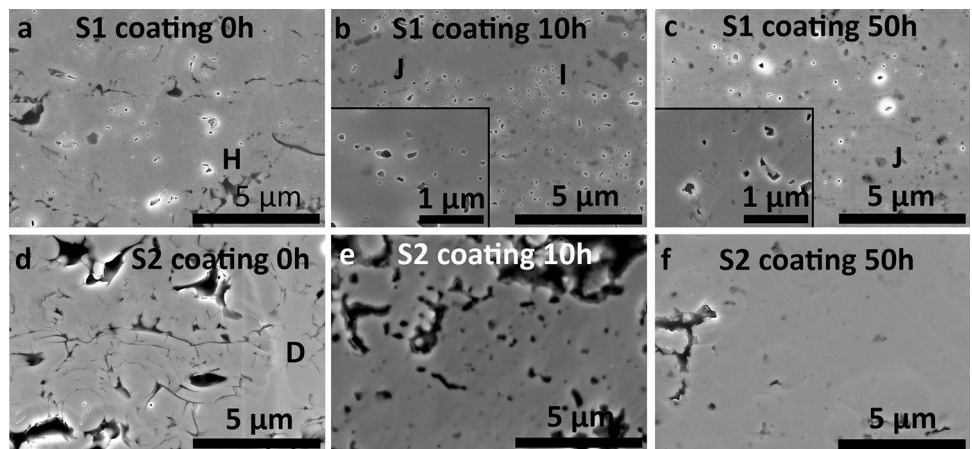


**Fig. 3** High-magnification SEM images of S1 and S2 coatings before heat treatment, after 10 and 50 hours heat treatment at 1150°C

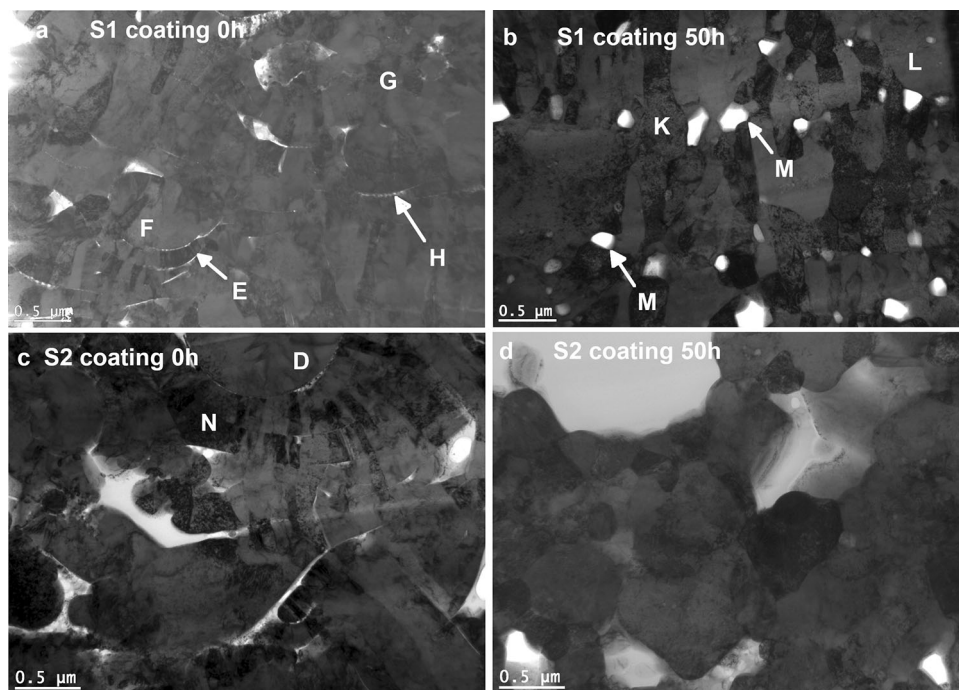


is equal to splat thickness and their width is 50-100 nm. The second group is formed by particles with a lower aspect ratio and larger thickness (F). Grains inside “E-type” particles are usually columnar; however, some equiaxial grains are observed as well (G). The relatively long gaps (H) between two successive splats are frequently

observed in both Fig. 3(a) and Fig. 4(a). The distance between those gaps usually is around 3-4 μm, which corresponds with the thickness of the coating deposited in one pass.

After heat treatment, porosity has been rearranged—globular pores underwent densification and either reduced

**Fig. 4** TEM images showing microstructure evolution of S1 and S2 coatings during annealing at 1150°C—the microstructure of the as-sprayed (a) and heat-treated for 50 hours (b) S1 coating, the microstructure of the as-sprayed and heat-treated S2 coating are presented in (c) and (d) images, respectively



their size (**I**)—while elongated intersplat voids tended to form bead-like porosity arrays (**J**). TEM image (Fig. 4b) reveals further details—the grains significantly coarsened, small columnar crystals inside splats transform into either large columns (**K**) or big equiaxial grains (**L**). Small polyhedral pores with a diameter of 100–300 nm were formed. Those pores tend to be surrounded by small equiaxial grains. It is likely that the change of the grain shape from columnar to equiaxed left behind free spaces. The pore formation at high temperature is further analyzed in the Discussion section. The dominant portion of pores' surfaces are convex (marked by arrows labeled with **M**) or flat, so one may anticipate that these pores will be stable during prolonged high-temperature exposure as discussed in (Ref 30, 31). Also, results published by other authors show the presence of pores in the YSZ TBC after several hundred (Ref 32–33) or even over one thousand (Ref 34) hours at high temperature.

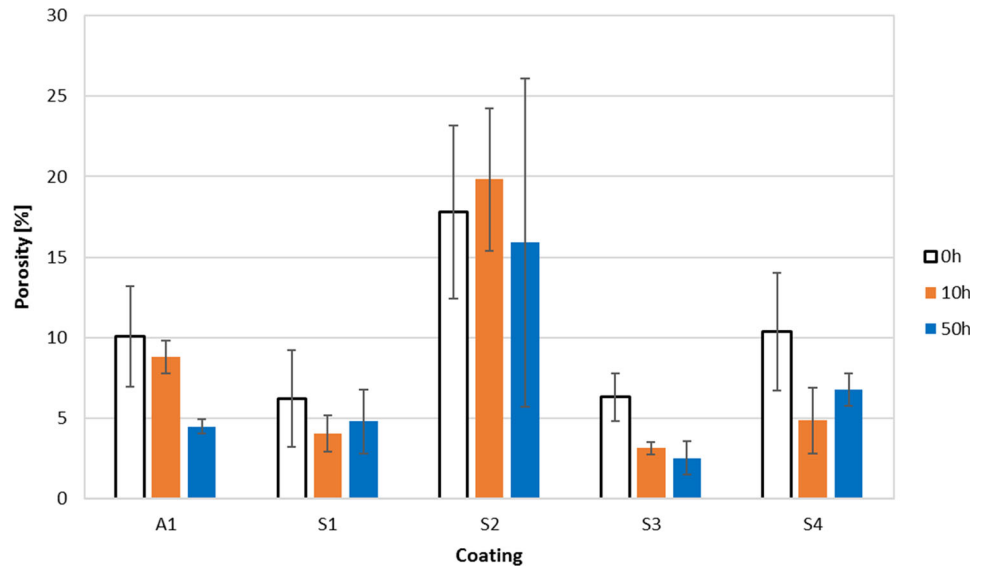
The high-magnification images (Fig. 3d and 4c) of the as-sprayed S2 coating reveal microstructure with relatively big pores, wide intersplat void/cracks and resolidified particles [Ref 15, 35]. Since these particles resolidified before reaching the substrate, they did not deform at impact to form splats, so they can be observed as spherical particles embedded in the coating (**D**). Despite longer spraying distance and lower deposition temperature, the wetting between splats was good as the TEM image (Fig. 4c) reveals areas (**N**) with lamellas sticking closely together. Inside such area columnar structure was developed with columns extending through several splats. Few narrow

intersplat gaps, typical for the S1 coating were observed. Some wide intersplat gaps were observed, and the notable feature of splats surrounding such gap is poorly developed columnar structure or even equiaxial grains.

Heat treatment of the S2 coating caused vanishing of the interlamellar voids without the formation of small pores (Fig. 3e, f), as it took place in the S1 coating. The big irregular pores visible in as-sprayed coating underwent spheroidization during heat treatment. TEM images (Fig. 4d) reveal more details about microstructure evolution, as the growth of primary columnar grains and the formation of coarse equiaxial grains.

Quantitative total porosity values obtained by image analysis of SEM images before and after heat treatment are presented in Fig. 5. The general trend toward densification is visible; however, slight porosity increase after 50 hours might have occurred for coatings S1 and S4, whereas the plasma-sprayed A1 coatings showed porosity decrease from the level of 10% to below 5% after 50 hours at 1150°C. This observation may be a result of large data scatter or growth of pores which were too small to be analyzed before. Cumulative pore size distributions of the five coatings are compared in Fig. 6. In the case of A1 voids with a diameter over 1 μm make a major contribution, only 1–2% percent of the total porosity is due to the finer pores below 1 μm in the as-sprayed coating and less than 1% for the coating after 50 hours at 1150°C. The A1 coating underwent significant densification by fine pore coalescence, so after extended heat treatment, only coarse porosity was observed. Heat treatment of the S1 and S3

**Fig. 5** Porosity variation during the heat treatment for 10 and 50 hours at 1150°C



coatings led to a decrease in the porosity from a level of about 7% to 5 and 3%, respectively. In contrast to the A1 coating, major porosity volume is due to very fine pores with a size of 500 nm and less. Heat treatment did not change it, and even after 10 or 50 hours at 1150°C, high density of very fine pores was observed (Fig. 3c).

In the case of the S2, the initial porosity was high—around 18%. The non-uniform microstructure of the S2 coating, however, caused notable variation of results among images. For instance, some images taken from inside of a column showed low porosity, while another taken from intercolumnar spaces showed much higher porosity. Thus, final porosity results show large scatter. Coarse pores with size from 1 to over 10  $\mu\text{m}$  contributed to most of the cumulated porosity; however, a relatively large fraction of pores with a size in the range from 400 nm to 1  $\mu\text{m}$  makes around 4% of the S2 coating porosity in the as-sprayed condition and after 10 hours of elevated temperature exposure. This fraction is greatly reduced by extended heat treatment.

The S4 coating showed porosity reduction from around 11% to 7% after heat treatment. Both fine (below 1  $\mu\text{m}$ ) and coarse pores contribute to the total porosity of the S4 coatings. Fine pores seem to be sintering-resistant as they remained as a significant fraction of all pores after 50 hours of high-temperature exposure.

In order to find the changes taking place in the specimens during the heat treatment, the freestanding coatings were broken by bending to reveal the details of splat and grain morphology. Figure 7 shows the fracture surfaces of the as-sprayed and heat-treated A1, S1 and S2 coatings. The conventional as-sprayed APS A1 coating was composed of well-adhered lamellar structures (splats). The columnar grains within the splats are visible (O), which

were formed because rapid nucleation occurred at impact when the bottom surface of the flattened droplet had been largely undercooled. The crystal grew rapidly opposite to the direction of heat flow forming such columnar grains. The microstructures of the as-sprayed SPS coatings S1 and S2 are shown in Fig. 7(c) and (e), respectively. Both images reveal microstructure formed by very fine splats with thickness around  $\sim 1\mu\text{m}$ . The columnar structure inside individual splats is visible (P), but it is not as clear as for the A1 coating. Defects like voids and intersplat cracks (Q) can be found in both coatings. In addition, near-spherical resolidified particles (R) are visible on the fractured surface of the S2 coating, which were formed due to the longer spraying distance, which allowed some molten particles time to cool down and solidify before impact. With extended exposure to high temperatures, all presented coatings (Figs. 7b, d and f) underwent sintering manifested in the growth of the intersplat contact area (Ref 36), healing-up of columnar grains (S) and interlamellar cracks. The sintering-led evolution of microstructure within the SPS coatings as observed by SEM was similar to the APS coating and no apparent differences, except splat size, could be identified.

XRD analysis was conducted on the freestanding APS and SPS coatings before and after heat treatment to check their phase stability. Spectra for the two most distinctive coatings, i.e., A1 (the lowest sintering shrinkage) and S2 (the highest shrinkage), are shown in Fig. 8a. These spectra demonstrate that the main phase in all the investigated coatings was a stable or metastable tetragonal  $t/t'$ - $\text{ZrO}_2$  phase. Such phase composition is typical for thermally sprayed YSZ coatings designed for TBC applications. In order to find minor phases which could be present in YSZ coatings such as monoclinic  $m$  and cubic  $c$ - $\text{ZrO}_2$ , detailed

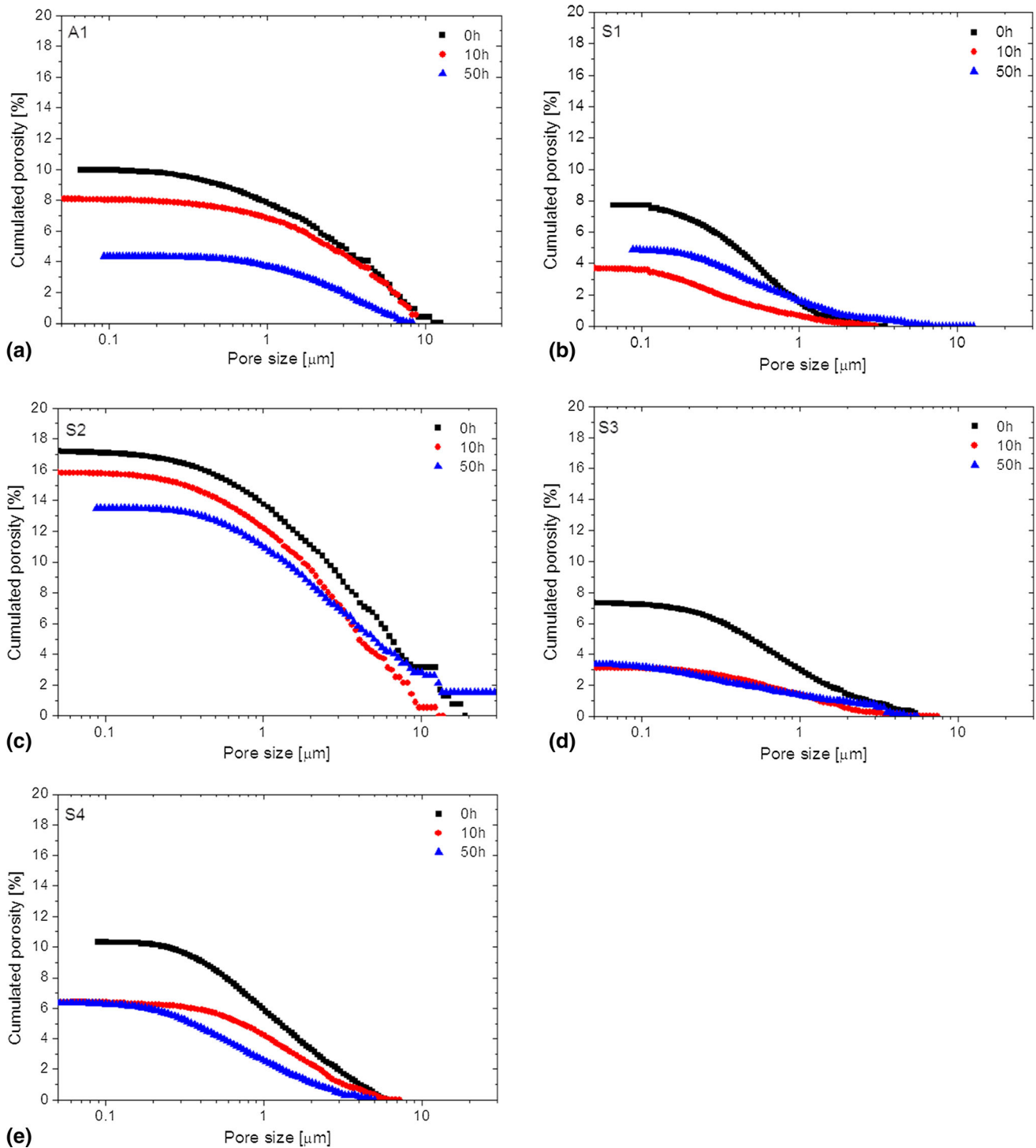


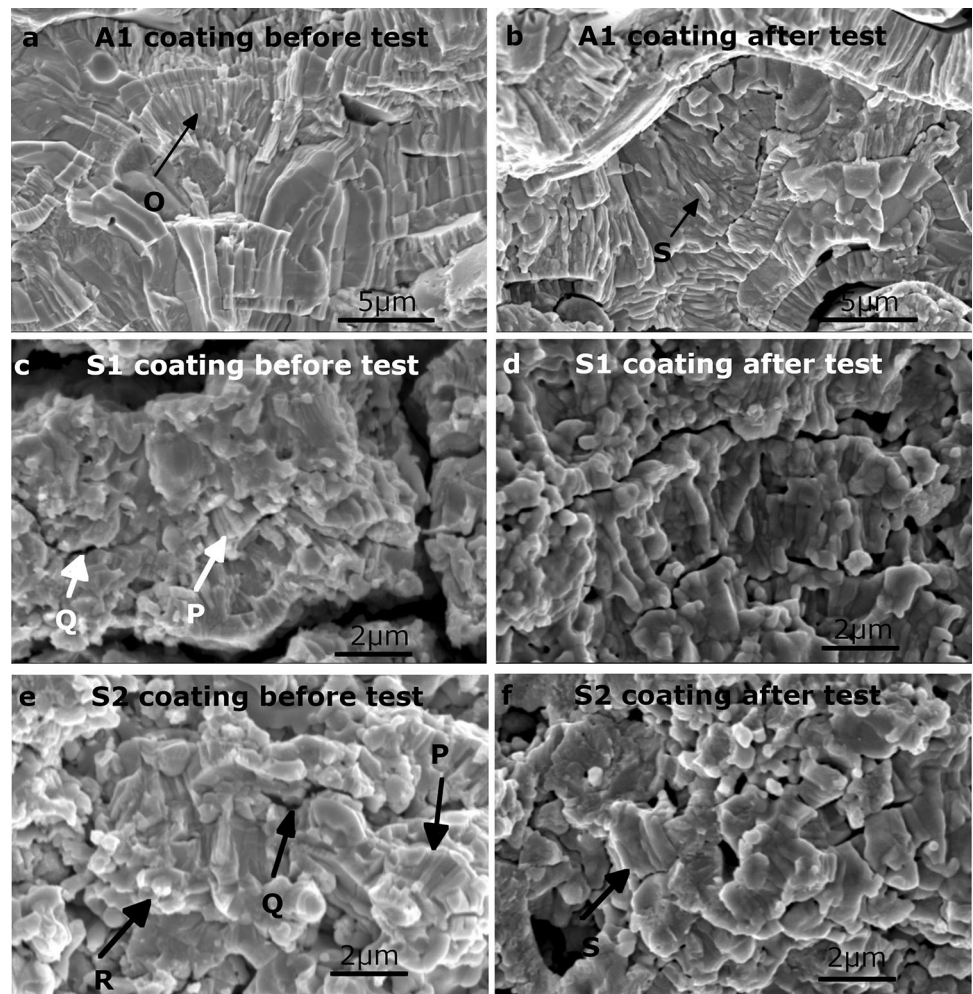
**Fig. 6** Cumulative distribution of pore size in the (a) A1, (b) S1, (c) S2, (d) S3 and (e) S4 coatings before and after heat treatment. Results obtained using Image Analysis of SEM pictures

scans with smaller step and longer exposure time were carried out in the range of  $26\text{--}36^\circ$  and  $72\text{--}76^\circ$ . Details about the diffraction peaks present in the range of  $2\theta = 26\text{--}36^\circ$  (Fig. 8b) show the absence of the monoclinic  $\text{ZrO}_2$  phase before as well as after heat treatment in the S2 coating.

Although some peaks of  $m\text{-ZrO}_2$  was detected in APS coatings before and after high-temperature exposure, the  $m\text{-ZrO}_2$  phase was found in the 204NS powder and it was passed to the coating. Nevertheless, it is unlikely that a very small ( $\sim 3\%$ ) amount of this thermally unstable phase



**Fig. 7** Fracture surface before (a,c,e) and after (b,d,e) dilatometry experiment. Images show typical features of the A1 (a,b), S1 (c,d) and S2 (e,f) coatings. The top of each image corresponds to the top of the coatings



influences thermomechanical properties of the coating. The detailed study of the peaks present in the range of  $2\theta = 72\text{--}76^\circ$  (Fig. 8c) indicates the presence of the tetragonal  $t\text{-ZrO}_2$  and  $t'\text{-ZrO}_2$  phases alone. Chen et al. (Ref 26) have reported the formation of the cubic  $c\text{-ZrO}_2$  phases after 100 h at  $1200^\circ\text{C}$  in SPS coatings, but in the current investigation, the cubic phase was not identified in any specimens.

Other SPS coatings were examined as well, but the obtained results were the same as for the S2 coating.

### Dilatometry

Dilatometry data are shown in Fig. 9. Measured expansion/contraction  $\Delta L/L_0$  of the five specimens was plotted against time with the temperature history. The average values of CTEs of all coatings are shown in Table 2. The calculated values are very similar around  $11 \cdot 10^{-6} \text{ K}^{-1}$ . Figure 10 shows the temperature–CTE relationship for all coating. The CTEs were calculated as slope of the expansion lines presented in Fig. 9. Also, in this case, individual

curves shear certain similarities. The CTE of YSZ coatings is expected to gradually rise in the temperature range between RT and  $\sim 1300^\circ\text{C}$ , such profile of YSZ coefficient of expansion has been reported before by, e.g., Haggerty et al. (Ref 37) and Baiamonte et al. (Ref 38). Indeed, arising values of CTE were observed between  $400$  and  $700^\circ\text{C}$  and over  $850^\circ\text{C}$ .

Between  $400$  and  $800^\circ\text{C}$ , the CTEs reached stable range and their values were about  $10 \cdot 10^{-6} \text{ 1}/^\circ\text{C}$ . The small hump is visible for temperature  $580\text{--}600^\circ\text{C}$ , which could be associated with the sintering of very fine pores with the size of several tens of nanometers at temperatures around  $700\text{--}800^\circ\text{C}$  (Ref 24). Over  $800^\circ\text{C}$  values of CTE started to rise. Such a profile of the YSZ coefficient of expansion has been reported before by, e.g., Haggerty et al. (Ref 37) and Baiamonte et al. (Ref 38). The further increase in the expansion coefficient is hindered by sintering-induced shrinkage in the S2, S3 and S4 coatings at temperatures over  $1000^\circ\text{C}$ . The sintering shrinkage affects the profile of the CTE–T line for the A1 and S1 coatings only at a high temperature close to  $1150^\circ\text{C}$ .

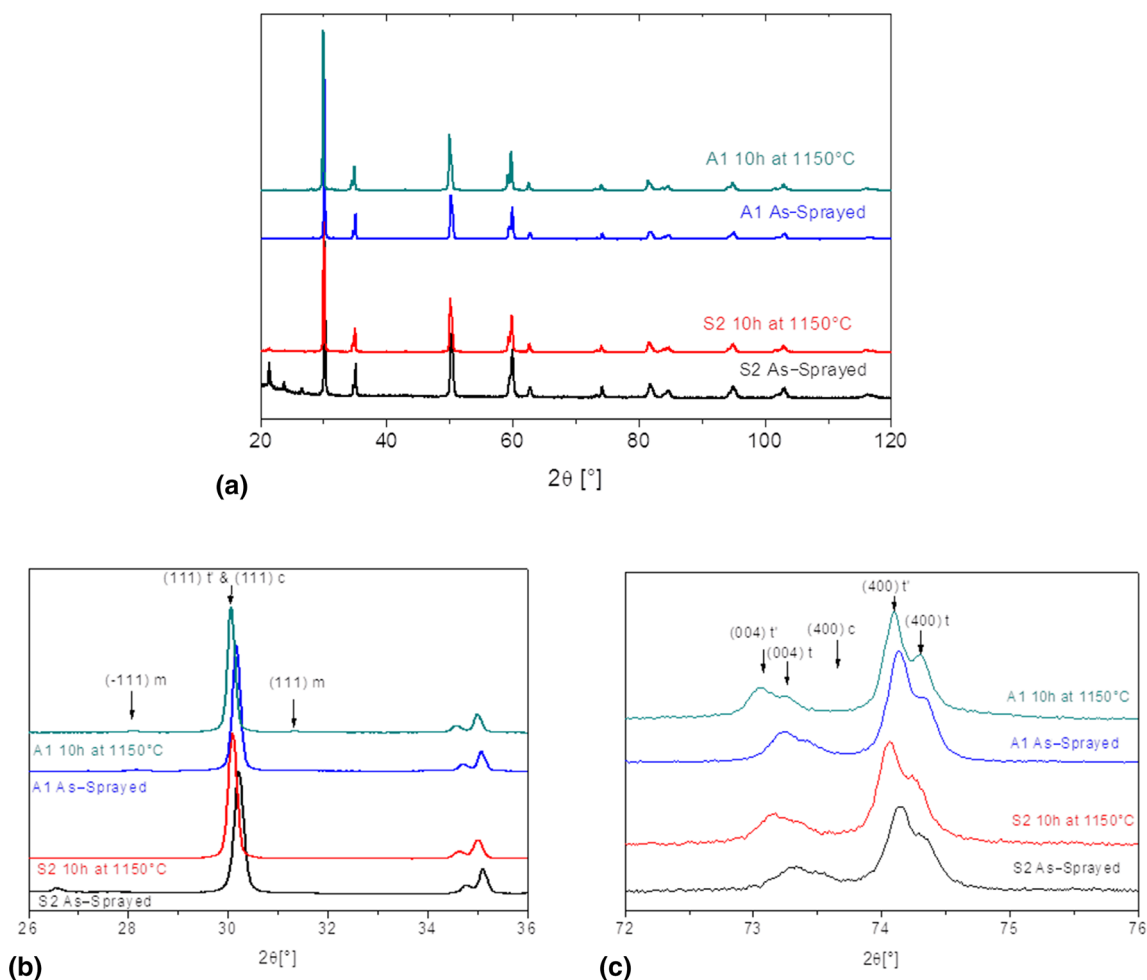


**Fig. 8** XRD spectra of the APS A1 and SPS S2 coatings before and after thermal heat treatment at 1150°C for 10h over  $2\theta = 20\text{--}120^\circ$ (a),  $26\text{--}36^\circ$ (b) and  $72\text{--}76^\circ$ (c), respectively

Although they showed similar expansion behavior during heating to 1150°C, it can be seen that sintering shrinkage varied significantly for the tested samples. Based on the plotted curves, the tested coatings could be divided into two groups. The A1 and S1 coatings form a class of coatings with a limited tendency to sinter (referred in this paper as *sintering-resistant*), while the S2, S3 and S4 coating belong to the family of coatings prone to shrinkage. In this work, the shrinkage  $\Sigma$  is defined as relative length change of the sample during the high-temperature exposure:

$$\Sigma = \frac{L_{0h}^{1150^\circ C} - L_{10h}^{1150^\circ C}}{L_{0h}^{25^\circ C}} \cdot 100[\%] \quad (\text{Eq 2})$$

For the sintering-resistant coatings, values of  $\Sigma$  are in the range of 0.1–0.2% (Table 2). The shrinkage of the coatings prone to sintering is about twice as high and can exceed 0.46%.

In order to take into account sintering-induced shrinkage which takes place in the range of temperature from 1000 to

1150°C, the corrected shrinkage parameter  $\Sigma_c$  is introduced. The corrected shrinkage is determined by lineary extrapolating the 600–800°C range of the curve up to 1150°C (Fig. 9c). The values of CTE, shrinkage and corrected shrinkage are listed in Table 2.

### Mechanical Properties

Table 3 shows the results of hardness and toughness measurements for all the tested coatings. The as-sprayed dense SPS coatings, S1 and S3 made with short spraying distance, had remarkably higher hardness than the APS coating. Due to the high porosity of the S2 coating, its hardness was the lowest, 7.9 GPa. Also, due to the refined microstructure (Ref 13) and good intersplat bonding, toughness of the dense SPS coatings was higher than that of the A1 coating, while the high porosity of S2 coatings had the lowest fracture resistance. As it is expected, the heat treatment increased both hardness and toughness of the APS coating. The observed changes are a result of the

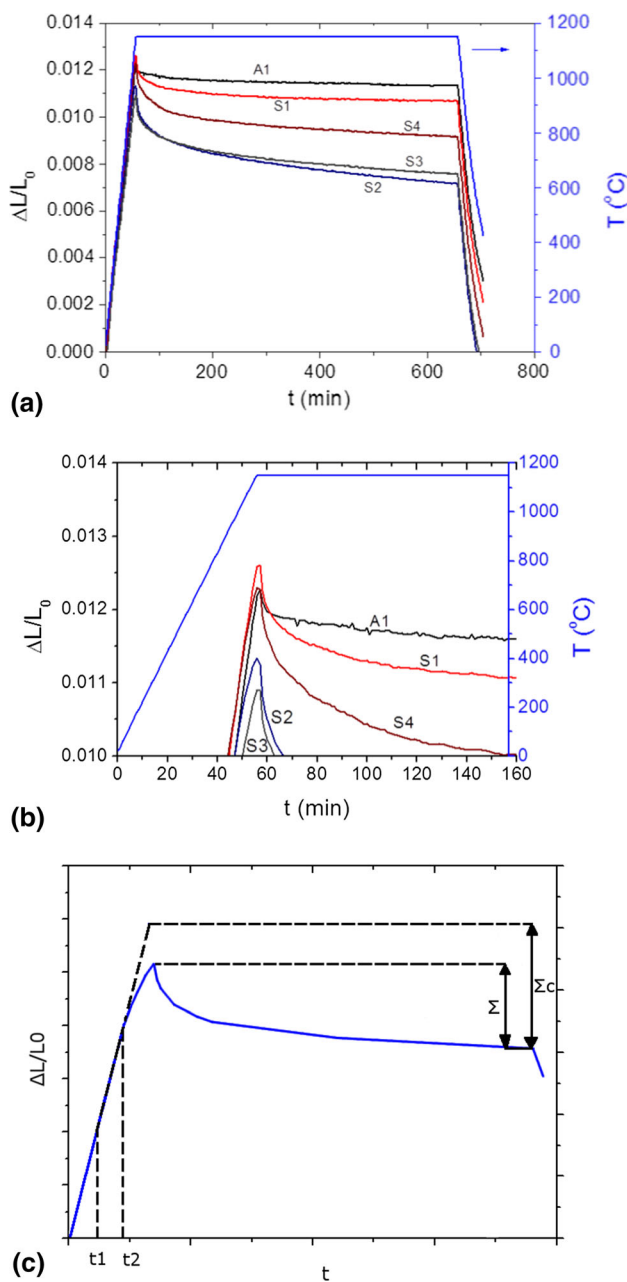


**Fig. 9** The temperature run and specimens' length change during the dilatometry test (a). Detailed insight into the initial part of the sintering curve (b). The method applied to determine corrected shrinkage value (c); points  $t_1$  and  $t_2$  correspond to the temperature of 600 and 800°C, respectively

**Table 2** Average values of thermomechanical parameters obtained in the dilatometry test

Coating	Mean CTE during heating $\times 10^{-6} [K^{-1}]$	Shrinkage $\Sigma$ [%]	Corrected Shrinkage $\Sigma_c$ [%]
A1	11.05	0.115	0.092
S1	11.19	0.198	0.180
S2	10.27	0.462	0.523
S3	10.43	0.343	0.370
S4	11.81	0.396	0.480

healing of microcrack, closure of pores and enhanced intersplat bonding (Ref 18). Surprisingly, however, the mechanical properties of the dense SPS coatings S1 and S3 deteriorated; in particular, the drop of toughness was significant. For S3 coating, for example, the very high initial value of  $2.83 \text{ MPa m}^{1/2}$  dropped to merely  $2.12 \text{ MPa m}^{1/2}$  after 50 hours at  $1150^\circ\text{C}$ . A similar evolution of both hardness and Young's modulus of SPS coatings was reported in (Ref 26). However, unlike the other SPS coatings heat treatment of S2 coatings caused an increase in both hardness and toughness in a similar manner as in the case of the A1 coating.

## Discussion

### Sintering and Evolution of Microstructure

The results presented hitherto show that changes of microstructure and properties of the APS and SPS coatings follow various paths depending upon their initial microstructure. Especially, the unique microstructure of the SPS coatings, which consists of very fine splats and sub-micron pores, results in intense shrinkage and often a peculiar evolution of the microstructure and properties of the coatings. Despite varying microstructures, results of the dilatometry experiment show that mean CTEs of all the tested coatings including both APS and SPS coating have values between  $10.3$  and  $11.8 \times 10^{-6} \text{ K}^{-1}$ . Such values are frequently reported for YSZ coatings. Also, an increase in CTE at a temperature above  $1000^\circ\text{C}$  is well known and was reported for instance by Baiamonte et al. (Ref 38) or Takagi et al. (Ref 24). Due to intense sintering at a temperature around  $1000^\circ\text{C}$ , this effect is not pronounced in some SPS coatings.

In many papers, authors have linked shrinkage of thermal sprayed YSZ coatings to their porosity. For instance, Vaßen et al. in (Ref 39) have established a simple linear relationship between shrinkage rate  $\Delta(L/L_0)/\Delta t$  and porosity  $P$  of coatings made of  $\text{ZrO}_2 - 8.36 \text{ mol.}\% \text{ Y}_2\text{O}_3 - 1.69\% \text{ HfO}_2$ :

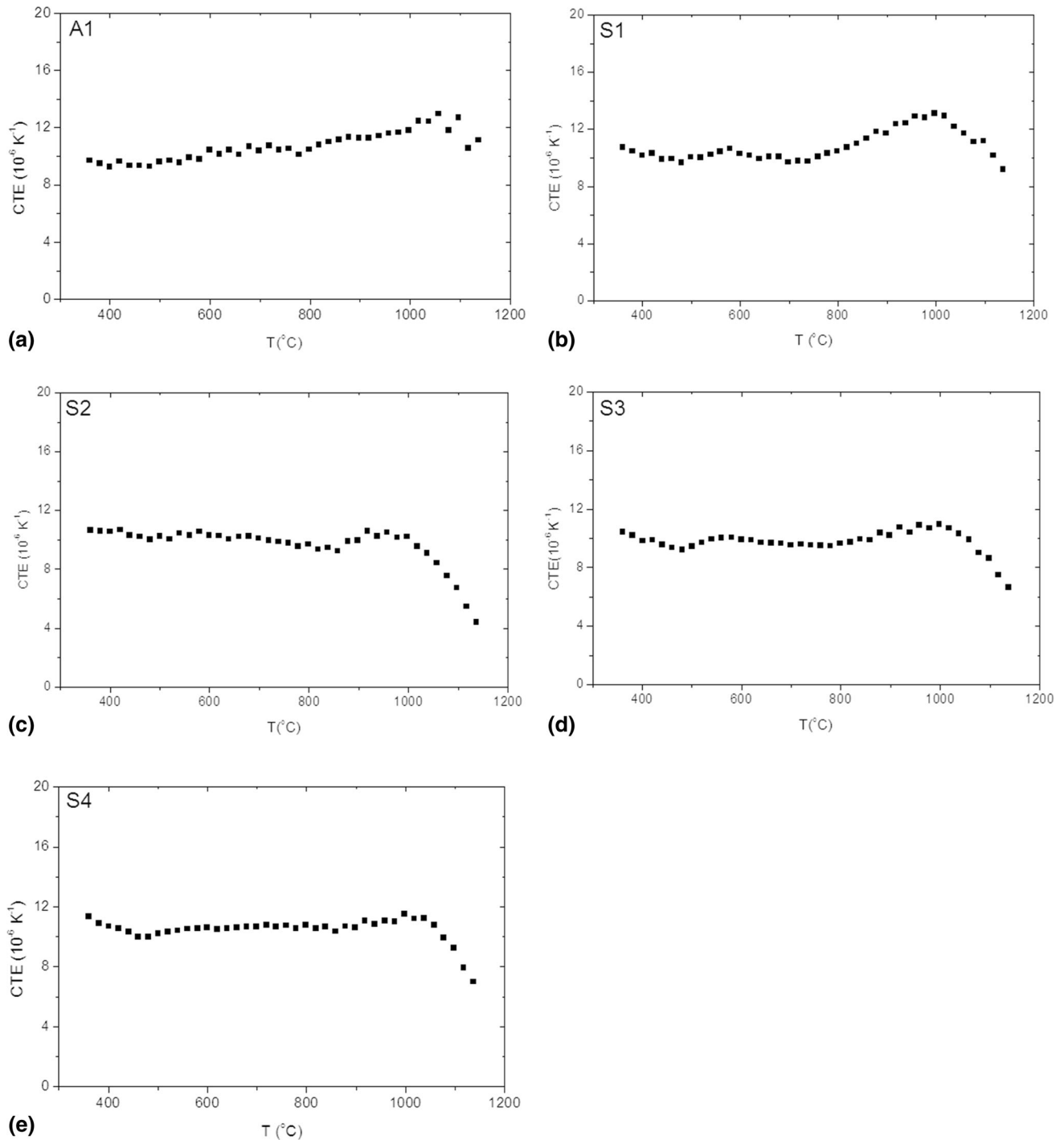


**Fig. 10** Temperature–CTE dependence of the (a) A1, (b) S1, (c) S2, (d) S3 and (e) S4 coatings

$$\frac{\Delta(l/l_0)}{\Delta t} = \alpha P \quad (\text{Eq 3})$$

where  $\alpha = 0.040 \pm 0.005$ , and  $l$  and  $l_0$  are the current and initial length of the sample.

Data presented in Table 2 and Fig. 7 suggest that in the present case such a simple approach is not satisfactory. For instance, the A1 coating with moderate porosity of 5%

showed a limited length contraction of only 0.09%, while the S4 coating with a similar level of total porosity showed significant shrinkage as high as 0.48%. To explain such a complex relationship between microstructures and shrinkage, mechanisms based on phase transformation, e.g., from  $t'$ -YSZ into mYSZ, could be ruled out as XRD did not reveal any change in phase composition. Advanced

**Table 3** Vickers hardness HV<sub>0.3</sub> and toughness for the coatings before and after 10h and 50h at 1150°C

Coating	Hardness [GPa]			Toughness [MPa m <sup>1/2</sup> ]		
	As-sprayed	10 h	50 h	As-sprayed	10h	50h
A1	8.1±1.1	8.6±0.9	8.7±1.0	2.60±0.83	2.70±0.81	2.93±0.80
S1	10.1±0.4	8.2±0.1	8.1±0.2	2.68±0.71	2.40±0.70	2.03±0.58
S2	7.9±0.9	8.1±0.6	8.2±0.5	2.22±0.62	2.32±0.65	2.56±0.69
S3	10.6±0.4	9.8±0.3	10.3±0.4	2.83±0.85	2.15±0.64	2.12±0.59
S4	8.4±0.2	8.6±0.6	8.6±0.4	2.95±0.80	2.66±0.72	2.36±0.61

sintering models, such as one proposed by Cipitria et al. (Ref 23, 40) and further developed by Takagi (Ref 24) take into account the geometry of splats and intersplat voids. The geometry considered in the model is shown in Fig. 11(a), where the elemental unit is single splat with radius  $r_s$  and thickness  $z$  connected to its neighbor by bridging. Between two splats there is an intersplat pore with thickness  $y$  and diameter  $r_p$ . Surface and grain boundary diffusion are considered as mechanisms for determining the high-temperature evolution of the microstructure. Other mechanisms such as lattice diffusion or viscous flow of liquid phases were neglected. Results of numerical calculations presented in (Ref 24) show that sintering is in a strong relationship with splat thickness  $z$  and pore size  $y$ , which is schematically shown in Fig. 11(b).

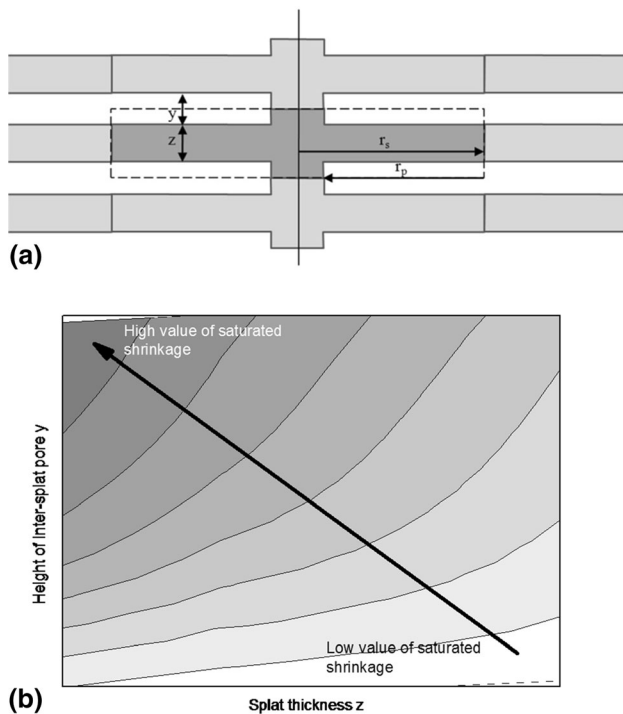


**Fig. 11** (a) Scheme of the geometry of splats in the numerical model proposed by Cipitria (Ref 23) and further developed by Takagi (Ref 24). (b) A scheme showing a change of saturated shrinkage with various splat thickness ( $z$ ) and height of intersplat pore ( $y$ ). Based on the numerical calculations of Takagi (Ref 24)

Microstructure consisting of thick splats together with narrow, disk-shaped, pores results in a low reduction in material’s volume due to shrinkage. The reduction in splat thickness and increase in the pore height lead to an increase in the sintering-driven contraction. In order to apply this model to the coatings investigated here, geometric parameters were evaluated and set together with shrinkage measured in the dilatometry test. The images of fractured surfaces provided information about splat thickness in each coating (Fig. 2). It is very difficult to properly evaluate pore size based on images of cross sections or fractured surfaces. Nevertheless, the porosity in the model is given by:

$$P = \frac{A_{\text{pores}}}{A_{\text{total}}} = \frac{r_p y}{r_s (y + z)} \tag{Eq 4}$$

Based on Fig. 3, 4 and 7, we can assume that the pore thickness is significantly smaller than the splat thickness  $y \ll z$ , which leads to:

$$P \approx \frac{r_p}{r_s z} y \tag{Eq 5}$$

Thus, we have assumed that the average pore size is related to total porosity, which allows us to plot sintering shrinkage data, average splat thickness and porosity on one graph (Fig. 12).

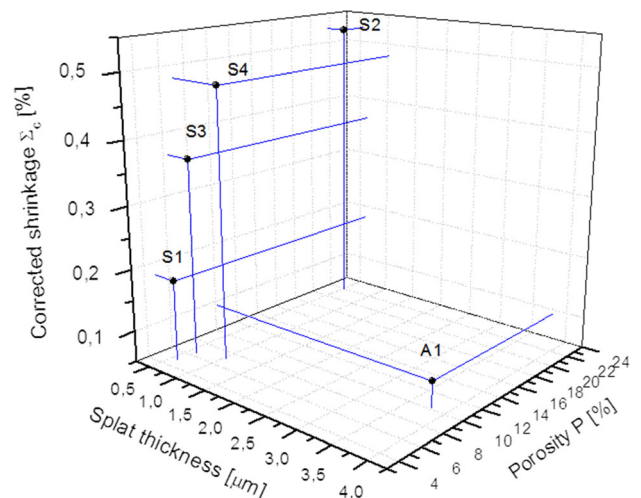


**Fig. 12** Dependence of corrected shrinkage of the tested coatings upon average splat thickness and initial porosity

Figure 12 shows two clear trends—a rapid increase in the sintering shrinkage with increasing coating porosity and with decreasing splat thickness. The increase seems to be substantial for porosity change from 4 to 8%, then it becomes moderate. Comparing coatings with similar porosity levels, i.e., the A1 and the S4 but with different splat thickness, it is clear that the coating with thicker splats shrinks significantly less. Keeping in mind that  $P \sim z_{s0}$  (Eq. 5), the presented results well correspond with calculations done by Takagi (Ref 24) and are schematically shown in Fig. 11(b).

The very low porosity of the S1 and S3 coatings should be an outcome of the short spraying standoff distance (Ref 41–43), which results in high velocity and temperature of particles. Thus, high values of hardness were reached. In order to find a cause of significantly higher hardness of the S3 coating, heat available for solid particle treatment were estimated. In this simple calculation, we have assumed that heat available  $Q$  for solid YSZ particles treatment is determined by power transferred to the plasma  $P$  decreased by enthalpy necessary for carrier liquid vaporization:

$$\frac{Q}{m_{YSZ}} = \frac{P - (1 - c)\dot{m}\Delta H_v}{c\dot{m}} \quad (\text{Eq 6})$$

where  $m_{YSZ}$  is mass of suspended YSZ particles,  $c$  is the concentration of solid particles in the suspension,  $\dot{m}$  is the suspension flow rate and  $\Delta H_v$  stands for the enthalpy change of vaporization (for water is 2.26 kJ/g and for ethanol is 0.84 kJ/g). Also, the assumption that ethanol combustion or pyrolysis do not take place has been made. The results are presented in Table 4. Heat available for YSZ particles under the S3 condition is much higher than in the S1; furthermore, it is well known that hydrogen-containing plasma has higher thermal conductivity (Ref 44), so one may expect ceramic particles better treated and hotter at impact. Formed splats can form more intimate bonding, which results in higher coating hardness. In the case of the S2 coating, at longer spraying distance the ceramic particles cooled down and resolidified. Figure 4 reveals plenty of spherical particles embedded in the

coating. With increasing spraying distance the plasma flow velocity decreases, so ceramic particles slow down too. Slower particles have lower kinetic energy at the impact that results in high porosity and low hardness of the S2 coating.

Application of water instead of ethanol as a liquid phase of the solution results in altered plasma jet–suspension interaction. Fragmentation of liquid stream depends on its Weber number. While suspension stream is breaking up, the mean droplet diameter  $d_d$  is given by

$$d_d = \frac{8\sigma}{C_D\rho u^2} \quad (\text{Eq 7})$$

where  $\sigma$  is the droplet surface tension,  $C_D$  is the flow drag coefficient,  $\rho$  is the plasma gas specific mass and  $u$  is the relative velocity between flow and droplet. Thus, the diameter of water to ethanol droplet is:

$$\frac{d_{d,\text{water}}}{d_{d,\text{ethanol}}} = \frac{\sigma_{\text{water}}}{\sigma_{\text{ethanol}}} = \frac{72\text{mN/m}}{22\text{mN/m}} = 3.27 \quad (\text{Eq 8})$$

and volume ratio:

$$\frac{V_{d,\text{water}}}{V_{d,\text{ethanol}}} = \left(\frac{d_{d,\text{water}}}{d_{d,\text{ethanol}}}\right)^3 = 35.05 \quad (\text{Eq 9})$$

It is clear that water-based suspension breaks up into significantly bigger droplets. Consequently one can expect that ceramic droplets will be accordingly bigger. At impact, ceramic particles flatten and average splat thickness is around 1  $\mu\text{m}$  which is twice as big as splat thickness in the coatings S1–S3. Big particles have high enough kinetic energy to form a dense coating with limited porosity ( $\sim 7\%$ ). Application of water also changes plasma enthalpy, and since water needs almost 3 times more heat to evaporate than ethanol, ceramic particles forming S4 coating are not well treated and might be cooler than those of the coating S3 (Table 4). Lower particle temperature may impede the formation of strong intersplat bonding, resulting in relatively low hardness.

Big (size of 1–5  $\mu\text{m}$ ) pores and narrow interlamellar voids contribute to the porosity of the SPS coatings. The

**Table 4** Spraying parameters and heat available for YSZ treatment

Coating	Solid/suspension %(wt.)	Powder/ Suspension feed rate g/min	Electrical power input kW	Net plasma power kW	Enthalpy of vaporization/ Plasma power %	Enthalpy/ suspension kJ/g	Enthalpy/ YSZ kJ/g
A1	.	19.5	26	9.0	.	.	27.7
S1	25	32	44.2	25.4	79	47.6	188.0
S2	25	32	44.2	25.4	79	47.6	188.0
S3	25	25	53.4	26.9	58	64.5	255.7
S4	25	37	58.8	29.6	78	48.0	189.5

former type is typical of coatings sprayed at long standoff distance (S2); however, sporadically such pores are present in denser SPS coatings. The large pores could be associated with low particle velocity and resolidification. After heat treatment, their size and shape barely changed. Much more interesting is a sintering behavior of interlamellar voids. Liu et al. (Ref 45) proposed a model of interlamellar pores sintering dependent on their opening width. According to the model, narrow pores, such as present in the coatings S1 and S3 (Fig. 4b, d and d), tend to disappear and form very small pores. The underlying mechanism is explained in Fig. 13(a). While heating, columnar grains inside the splat gradually transform into equiaxial grains and as result pore surfaces roughen. If the lamellar pore is narrow enough, the opposite protrusions can form bridges across the pore. Then mass transport from the concave pore surface toward convex pore surfaces takes place. Finally, a bead-like array of very small spherical pores (Fig. 5f) with the size of a few tens or hundreds of nanometers is formed. Similar models was also reported in (Ref 46–47).

In contrast, wide interlamellar pores like those present in the A1 and S2 (clearly visible in Fig. 5d) and occasionally in the S4 tend to prevent bridging. At high temperature, while surfaces experience roughening, the height of the protrusion is too small to contact opposing protrusion (Fig. 13b). In such a case, the surface of the entire pore is an easy path for diffusion; thus, the sintering results in rather big spherical pore located in virtually poreless

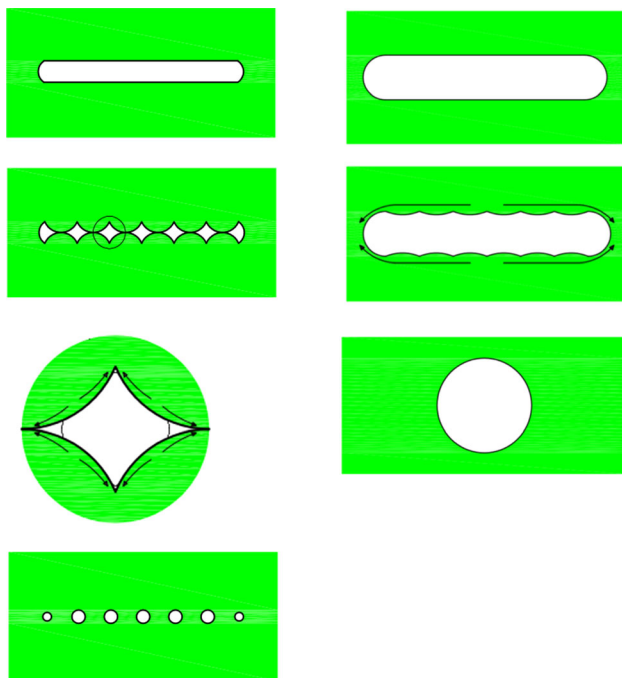


**Fig. 13** Porosity evolution during high-temperature exposure. Sintering of the pore with small (a) and large (b) opening width. Based on Liu et al. (Ref 45)

material, which is shown in Fig. 5(f). Various pore arrangements could affect the mechanical properties of the coatings, including hardness. Nevertheless, the mechanism behind these changes is not fully understood yet and will be a subject of a more detailed study.

### Changes of mechanical properties

Various paths of porosity evolution are expected to lead to different changes of mechanical properties. Particularly interesting analysis of this effect was described by Leguillon and Piat in (Ref 48). The authors investigated several pores' arrangements, shapes and orientations using both the energy and stress conditions of crack propagation. The presence of pores in front of the crack has two contradictory effects—weakening effect caused by a decreasing volume of solid material and, on the other hand, the crack blunting due to the pore resulting in an apparent toughness enhancement and decrease in the effective Young's modulus. The normalized distance between two cracks  $\zeta$  (normalized by the pore diameter) affects the toughness of the ceramics—for the small distance between cracks significant weakening was predicted; with the longer distance, toughness of the porous material can overcome fracture resistance of the dense material. Also, it was found that pore size has an influence on weakening/strengthening effect—calculation for alumina with a pore size of 100  $\mu\text{m}$  showed that it could be tougher than alumina with pores of 10  $\mu\text{m}$  in diameter. For even smaller pores ( $d \approx 1 \mu\text{m}$ ) toughening cannot be observed. Deng et al. (Ref 49) investigated fracture toughness of two porous SiC ceramics with the same density but various pore sizes. Both analytical study and experimental results showed that the larger pore size at the crack front results in the higher fracture toughness of the ceramic relative to fracture strength of material with finer pores. Jauffres et al. (Ref 50) simulated the toughness change of two ceramics using the discrete element method. For a given porosity, the ceramic sintered from the green body with lower density showed higher toughness due to better bonding between sintered particles.

The porosity–crack relationship established by Leguillon and Piat in the paper (Ref 48) may well correspond with the results presented in this work. Very fine pores (Fig. 5b, c and Fig. 6b) if located at the crack front may affect the coating's fracture resistance and eventually lead to ceramic embrittlement. To verify that claim, the TBCs' toughness was plotted together with an average distance between two pores.

Using image analysis, qualitative data on porosity were extracted, so mean pore–pore distance  $\lambda$  was calculated using equation (see “Appendix A” to check how the equation was derived):

$$\lambda = Y \frac{d}{\sqrt{P}} \quad (\text{Eq 10})$$

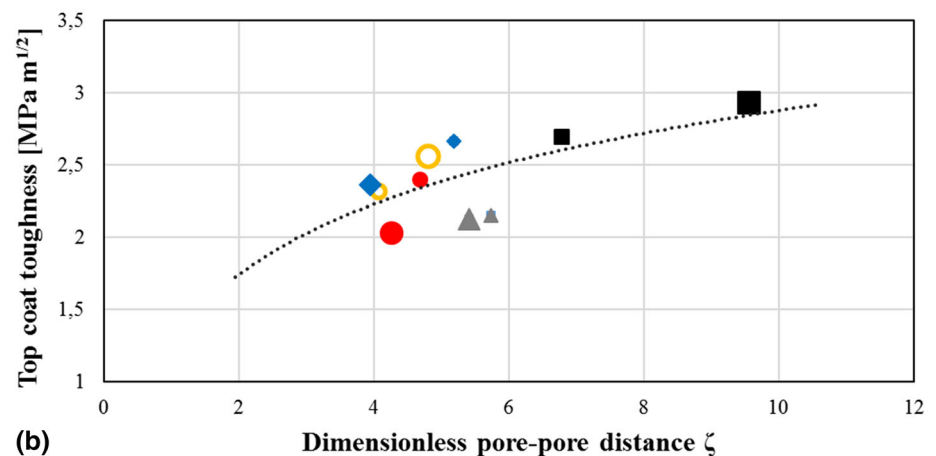
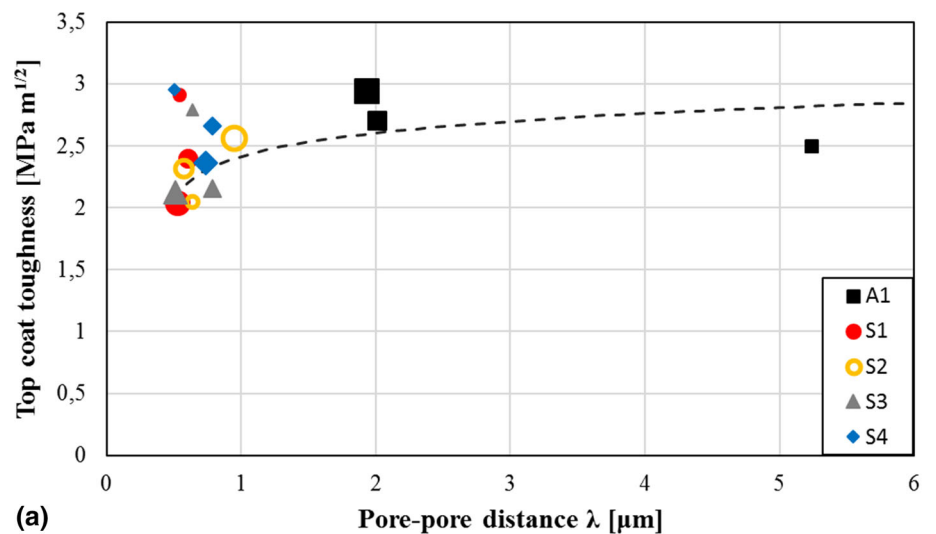
where  $Y$  is a parameter depending on assumed geometry of pore arrangements,  $d$  is an average pore size and  $P$  stands for porosity.

Plotting  $\lambda$  against top coatings' toughness shows how the evolution of microstructure affects mechanical properties. Data points presented in Fig. 14(a) do not show a strong relation between  $\lambda$  and  $K_{\text{VIF}}$ ; however, it is worth noticing that most points which are located far from expected fitting line represent properties of the coatings in as-sprayed condition (indicated by arrows). Taking only heat-treated coatings into account, closer relationship is seen (Fig. 14b)—with increasing dimensionless distance  $\zeta(\lambda/d)$  between pores toughening of ceramic material is observed—as it was predicted by Leguillon and Piat. Particularly, it is well seen for points representing the same type of coatings. The changes in the microstructure during heat treatment could lead either toward pore coalescence and growth or refinement, as it was shown in Section 5.8;

thus, coating could become tougher or more brittle, respectively.

The reason why the as-sprayed coating did not follow the pattern is unclear. Some possible explanations could be proposed though. At first, pores in the as-sprayed coatings usually take the form of flat voids between two overlaying splats (Fig. 6a and c), microcracks or irregular voids where impacting droplet did not fill asperities on coating's surface or interpass porosity bands. Such shape and arrangement of pores in the as-sprayed coatings make them very different than pores in the heat-treated coating, which have a more globular shape (Fig. 6b and d). Microcracks and highly oblate voids modify the stress field in the coating (Ref 51–52) and could lead to crack deflections and branching. Another explanation may be quality of bonding between two adjacent splats as better intersplat cohesion results in high toughness of coating. The bonding quality strongly depends on the spraying parameters and particle in-flight properties (temperature, velocity) (Ref 53). After high-temperature exposure cohesion between splats is affected

**Fig. 14** Effect of pore–pore distance on the toughness of (a) all tested and (b) only heat-treated top coatings. The size of the symbols corresponds to heat treatment time, small represents as-sprayed condition without heat treatment, midsize and large stand for 10 and 50 hours at 1,150°C, respectively. In the presented plot,  $Y=0.58$  (corresponding to the hexagonal porosity arrangement) was taken into account





by sintering and resulting microstructure (Ref 18, 54). Yet another explanation may include various grain structure of the coating before and after heat treatment. In the as-sprayed coating, each splat typically consists of columnar crystals which after sintering take more equiaxed form. Finally, compressive residual stress present in the as-sprayed coatings may increase fracture toughness by crack closing (Ref 48, 55). Reduction in coating’s toughness was considered as one of the main factors leading to a decrease in the thermal shock resistance of the SPS coatings that was reported by authors in (Ref 56). The origin of peculiar hardness changes (softening) is not well known and should be further investigated.

Very fine porosity in aged SPS coatings was reported in many papers like (Ref 57, 58) or study based on USAXS measurements published by Bacciochini et al. in (Ref 25, 59), though the authors did not pay close attention to it or did not try to explain its origins.

### Conclusions

Sintering of the ceramic top coatings in TBC systems is known to be one of the most important factors causing their failure. As compared with coatings sprayed by APS, these made by SPS have very distinctive microstructures, including finer splats and submicron porosity. The distinctive microstructures of the SPS coatings cause variations in thermomechanical properties which can be summarized in the followings:

- The mean values of CTE are between 10.27 and 11.81  $\times 10^{-6} \text{ K}^{-1}$  and they seem not to be related to the coating microstructure. The CTE is not constant in the range of temperature from RT to 1150°C—the value of the CTE rises with increasing temperature. In the case of SPS coatings, intense shrinkage at a temperature around 1000°C hinders increasing CTE value above this range.
- The sintering shrinkage depends on both splat size (thickness) and coating porosity. Splats in the SPS coatings possess very small thickness (0.5-1.0  $\mu\text{m}$ ), which promotes significant sintering shrinkage even if coatings are relatively dense (porosity around 8% and less).
- Various paths of porosity rearrangement may lead to very different changes of coatings’ mechanical properties. Formation of arrays of fine pores can lead to coating embrittlement as observed for the coatings S1, S3 and S4. On the other hand, densification with the formation of fewer but larger, spherical pores as observed for the A1 and S2 coatings leads to toughening.

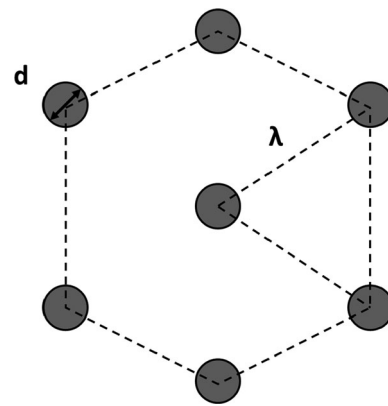


**Fig. 15** Hexagonal pores arrangement used to find the distance between two neighbor pores

### Appendix

The distance was estimated using a simplified model of the hexagonal pores arrangement (Fig. 15).

The total area of  $n$  pores with diameter  $d$  in the considered portion of the porous coating with porosity  $p$  and area  $A$  is given by

$$n \frac{\pi d^2}{4} = PA \tag{Eq A1}$$

For hexagonal arrangement  $A = \frac{3\sqrt{3}}{2} \lambda^2$  and  $n = 2$ , so

$$2\pi d^2 = 6\sqrt{3}\lambda^2 P \tag{Eq A2}$$

And finally

$$\lambda^2 = \frac{\sqrt{3}\pi d^2}{9 P} \tag{Eq A3}$$

Similar calculations for another arrangement of pores (such as square or three-dimensional cubic) result in a similar relationship with various proportionality factor; thus, distance  $\lambda$  may be given in general by:

$$\lambda = Y \frac{d}{\sqrt{P}} \tag{Eq A4}$$

where  $Y$  is constant dependent on considered geometry.

**Acknowledgments** The authors acknowledge the contribution of Dr. Keiko Suzuta from NIMS, who carried out the dilatometry experiment, Ms. Nina Dusautoy from École Nationale Supérieure d’Ingénieurs in Limoges, France, who assisted in the spraying processes, specimen preparation and measurements, Dr. Tomasz Płociński and Dr. Piotr Bazarnik from Warsaw University of Technology for guidance on electron microscopy investigations and sample preparation. This work was carried out as a part of NIMS-WUT Joint Graduate Program.

## References

1. R. Miller, Thermal Barrier Coatings for Aircraft Engines: History and Directions, *J. Therm. Spray Technol.*, 1995, **6**, p 32–42.
2. D. Zhu and R.A. Miller, Thermal-Barrier Coatings for Advanced Gas-Turbine Engines, *MRS Bullet.*, 2000, **27**, p 43–47.
3. U. Schulz, S. Saruhan, K. Fritscher and C. Leyens, Review on Advanced EB-PVD Ceramic Topcoats for TBC Applications, *Int. J. Appl. Ceram. Technol.*, 2004, **1**, p 302–315.
4. R. Vassen, M. Jarligo, T. Steinke, D.E. Mack and D. Stover, Overview on Advanced Thermal Barrier Coatings, *Surf. Coat. Technol.*, 2010, **205**, p 938–942.
5. X.Q. Cao, R. Vassen and D. Stöver, Ceramic Materials for Thermal Barrier Coatings, *J. Eur. Ceram. Soc.*, 2004, **24**, p 1–10.
6. D.R. Clarke and S.R. Phillpot, Thermal Barrier Coating Materials, *Mater. Today*, 2005, **8**, p 22–29.
7. D.R. Clarke, M. Oechsner and N.P. Padture, Thermal-Barrier Coatings for More Efficient Gas-Turbine Engines, *MRS Bull.*, 2012, **37**, p 891–898.
8. G. Mauer, M.O. Jarligo, D.E. Mack and R. Vaßen, Plasma-Sprayed Thermal Barrier Coatings: New Materials, Processing Issues, and Solutions, *J. Therm. Spray Technol.*, 2013, **22**, p 646–658.
9. G. Mauer, A. Hospach and R. Vaßen, Process Development and Coating Characteristics of Plasma Spray-PVD, *Surf. Coat. Technol.*, 2013, **220**, p 219–224.
10. X. Ma, F. Wu, J. Roth, M. Gell and E.H. Jordan, Low Thermal Conductivity Thermal Barrier Coating Deposited by the Solution Plasma Spray Process, *Surf. Coat. Technol.*, 2006, **201**, p 4447–4452.
11. A.D. Jadhav, N.P. Padture, E.H. Jordan, M. Gell, P. Miranzo and E.R. Fuller Jr., Low- Thermal-Conductivity Plasma-Sprayed Thermal Barrier Coatings with Engineered Microstructures, *Acta Mater.*, 2006, **54**, p 3343–3349.
12. P. Blazdell and S. Kuroda, Plasma Spraying of Submicron Ceramic Suspensions Using a Continuous Ink Jet Printer, *Surf. Coat. Technol.*, 2000, **123**, p 239–246.
13. P. Fauchais, A. Joulia, S. Goutier, C. Chazelas, M. Vardelle, A. Vardelle and S. Rossignol, Suspension and Solution Plasma Spraying, *J. Phys. D: Appl. Phys.*, 2013, **46**, p 224015–224028.
14. A. Guignard, G. Mauer, R. Vassen and D. Stöver, Deposition and Characteristics of Submicrometer Structured Thermal Barrier Coatings by Suspension Plasma Spraying, *J. Therm. Spray Technol.*, 2012, **21**, p 416–424.
15. X. Chen, S. Kuroda, T. Ohnuki, H. Araki, M. Watanabe and Y. Sakka, Effects of Processing Parameters on the Deposition of Yttria Partially Stabilized Zirconia Coating During Suspension Plasma Spray, *J. Amer. Ceram. Soc.*, 2016, **10**, p 1–10.
16. X. Chen, H. Honda, S. Kuroda, H. Araki, H. Murakami, M. Watanabe and Y. Sakka, Highly Segmented Thermal Barrier Coatings Deposited by Suspension Plasma Spray: Effects of Spray Process on Microstructure, *J. Therm. Spray Technol.*, 2016, **25**, p 1638–1649.
17. B. Siebert, C. Funke, R. Vaßen and D. Stover, Changes in Porosity and Young's Modulus Due to Sintering of Plasma Sprayed Thermal Barrier Coatings, *J. Mater. Process. Technol.*, 1999, **92–93**, p 217–223.
18. Y. Yamazaki, A. Schmidt and A. Scholz, The Determination of the Delamination Resistance in Thermal Barrier Coating System by Four-Point Bending Tests, *Surf. Coat. Technol.*, 2006, **201**, p 744–754.
19. J.B. Huang, W.Z. Wang, Y.J. Li, H.J. Fang, D.D. Ye, X.C. Zhang and S.T. Tu, Novel-Structured Plasma-Sprayed Thermal Barrier Coatings with low Thermal Conductivity, High Sintering Resistance and High Durability, *Ceram Int*, 2021, **47**, p 5156–5167.
20. X. Zhung, A.C.F. Cocks, Y. Okajima, K. Takeno and T. Torigoe, An Image-Based Model for the Sintering of Air Plasma Sprayed Thermal Barrier Coatings, *Acta Mater*, 2021, **206**, p 116649.
21. E.J. Gildersleeve and S. Sampath, Durability of Plasma Sprayed Thermal Barrier Coatings with Controlled Properties Part I: For Planar Disk Substrates, *Surf Coat Technol*, 2021, **424**, p 127678.
22. H.E. Eaton and R.C. Novak, Sintering Studies of Plasma-Sprayed Zirconia, *Surf. Coat. Technol.*, 1987, **32**, p 227–236.
23. A. Cipitria, I.O. Golosnoy and T.W. Clyne, A Sintering Model for Plasma-Sprayed Zirconia TBCs Part I: Free-Standing Coatings, *Acta Mater.*, 2009, **57**, p 980–992.
24. K. Tagaki, D. Kudo, A. Kawasaki and Y. Harada, Microstructural Dependency of Thermal Expansion and Sintering Shrinkage in Plasma-Sprayed Zirconia Coatings, *Surf. Coat. Technol.*, 2011, **205**, p 4411–4417.
25. A. Bacciochini, F. Ben-Ettouil, E. Brousse, J. Ilavsky, G. Montavon, A. Denoirjean, S. Valette and P. Fauchais, Quantification of Void Networks of as-Sprayed and Annealed Nanostructured Yttria-Stabilized Zirconia (YSZ) Deposits Manufactured by Suspension Plasma Spraying, *Surf. Coat. Technol.*, 2010, **205**, p 683–689.
26. X. Chen, T. Ohnuki, S. Kuroda, M. Gizynski, H. Araki, H. Murakami, M. Watanabe and Y. Sakka, Columnar and DVC-Structured Thermal Barrier Coatings Deposited by Suspension Plasma Spray: High-Temperature Stability and Their Corrosion Resistance to the Molten Salt, *Ceram. Int.*, 2016, **42**, p 16822–16832.
27. J. Sniezewski, V. Vidal, P. Lours and Y. Le Maoult, Thermal Barrier Coatings Adherence and Spallation: Interfacial Indentation Resistance and Cyclic Oxidation Behaviour Under Thermal Gradient, *Surf. Coat. Technol.*, 2009, **204**, p 807–811.
28. J. Lesage and D. Chicot, Role of Residual Stresses on Interface Toughness of Thermally Sprayed Coatings, *Thin Solid Films*, 2002, **415**, p 143–150.
29. G.R. Anstins, P. Chantikul, B.R. Lawn and D.B. Marshal, A Critical Evaluation of Indentation Techniques for Measuring Fracture Toughness: I, Direct, Crack Measurements, *J. Amer. Ceram. Soc.*, 1981, **64**, p 533.
30. B.J. Kellett and F.F. Lange, Thermodynamics of Densification: I, Sintering of Simple Particle Arrays, Equilibrium Configurations, Pare Stability, and Shrinkage, *J. Amer. Ceram. Soc.*, 1989, **72**, p 725–734.
31. L.C. de Jonghe and M.N. Rahaman, Sintering of Ceramics, *Handbook of Advanced Ceramics: Materials, Applications, Processing and Properties*. S. Somiya Ed., Elsevier Inc., Amsterdam, 2013, p 187–264
32. A. Ganvir, N. Markoscan and S. Joshi, Influence of Isothermal Heat Treatment on Porosity and Crystallite Size in Axial Suspension Plasma Sprayed Thermal Barrier Coatings for Gas Turbine Applications, *Coat.*, 2017, **7**, p 4–17.
33. N. Zotov, M. Bartsch and G. Eggeler, Thermal Barrier Coating Systems—Analysis of Nanoindentation Curves, *Surf. Coat. Technol.*, 2009, **203**, p 2064–2072.
34. J.D. Osorio, D. Maya, A.C. Barrios, A. Lopera, F. Jimenez, J.M. Meza, J.P. Hernandez-Ortiz and A. Toro, Correlations Between Microstructure and Mechanical Properties of Air Plasma-Sprayed Thermal Barrier Coatings Exposed to a High Temperature, *J. Amer. Ceram. Soc.*, 2013, **96**, p 3901–3907.
35. Y.P. Wan, V. Prasad, G.X. Wang, S. Sampath and J.R. Fincke, Model and Powder Particle Heating Melting, Resolidification, and Evaporation in Plasma Spraying Processes, *J Heat Transfer*, 1999, **121**, p 691–699.
36. I.O. Golosnoy, S.A. Tsipas and T.W. Clyne, An Analytical Model for Simulation of Heat Flow in Plasma-Sprayed Thermal Barrier Coatings, *J. Therm. Spray Technol.*, 2005, **14**, p 205–214.

37. R.P. Haggerty, P. Sarin, Z.D. Apostolov, P.E. Driemeyer and W.M. Kriven, Thermal Expansion of HfO<sub>2</sub> and ZrO<sub>2</sub>, *J. Amer. Ceram. Soc.*, 2014, **97**, p 2213-2222.
38. L. Baiamonte, F. Marra, G. Pulci, J. Tirillò, F. Sarasini, C. Bartuli and T. Valente, High Temperature Mechanical Characterization of Plasma-Sprayed Zirconia-Yttria From Conventional and Nanostructured Powders, *Surf. Coat. Technol.*, 2015, **277**, p 289-298.
39. R. Vaßen, N. Czech, W. Mallener, W. Stamm and D. Stover, Influence of Impurity Content and Porosity of Plasma-Sprayed Yttria-Stabilized Zirconia Layers on the Sintering Behavior, *Surf. Coat. Technol.*, 2001, **141**, p 135-140.
40. A. Cipitria, I.O. Golosnoy and T.W. Clyne, A Sintering Model for Plasma-Sprayed Zirconia Thermal Barrier Coatings Part II: Coatings Bonded to a Rigid Substrate, *Acta Mater.*, 2009, **57**, p 993-1003.
41. X.M. Shao, K. Zhang and H.B. Xiong, Modeling of Micro- and Nanoparticle Characteristics in DC Suspension Plasma Spray, *J. Therm. Spray Technol.*, 2015, **24**, p 309-317.
42. O. Marchand, L. Girardot, M.P. Planche, P. Bertrand, Y. Bailly and G. Bertrand, An Insight into Suspension Plasma Spray: Injection of the Suspension and Its Interaction with the Plasma Flow, *J. Therm. Spray Technol.*, 2011, **20**, p 1310-1320.
43. C. Delbos, J. Fazilleau, V. Rat, J.F. Coudert, P. Fauchais and B. Pateyron, Phenomena Involved in Suspension Plasma Spraying Part 2: Zirconia Particle Treatment and Coating Formation, *Plasma Chem. Plasma Process.*, 2006, **26**, p 393-414.
44. M. Boulos, P. Fauchais and E. Pfender, *Thermal plasmas, fundamentals and application*, 1st ed. Plenum Press, New York and London, 1994.
45. T. Liu, X.T. Luo, X. Chen, G.J. Yang, C.X. Li and C.J. Li, Morphology and Size Evolution of Interlamellar Two-Dimensional Pores in Plasma Sprayed La<sub>2</sub>Zr<sub>2</sub>O<sub>7</sub> Coatings During Thermal Exposure at 1300C, *J. Therm. Spray Technol.*, 2015, **24**, p 739-748.
46. D.G.R. Li, L.S. Wang, G.J. Yang, C.X. Li and C.J. Li, Combined Effect of Internal and External Factors on Sintering Kinetics of Plasma-Sprayed Thermal Barrier Coatings, *J Europ Ceram Soc*, 2019, **39**, p 1860-1868.
47. B. Lv, X. Fan, H. Xie and T.J. Wang, Effect of Neck Formation on the Sintering of Air-Plasma-Sprayed Thermal Barrier Coating System, *J Europ Ceram Soc*, 2017, **37**, p 811-821.
48. D. Leguillon and R. Piat, Fracture of Porous Materials - INFLUENCE of the Pore Size, *Eng. Fract. Mech.*, 2008, **75**, p 1840-1853.
49. Z.Y. Deng, J. She, Y. Inagaki, J.F. Yang, T. Ohji and Y. Tanaka, Reinforcement by Crack-Tip Blunting in Porous Ceramics, *J. Eur. Ceram. Soc.*, 2004, **24**, p 2055-2059.
50. D. Jauffres, C.L. Martin, A. Lichtner and R.K. Bordia, Simulation of the Toughness of Partially Sintered Ceramics with Realistic Microstructures, *Acta Mater.*, 2012, **60**, p 4685-4694.
51. S. Kuroda and T.W. Clyne, The Quenching Stress in Thermally Sprayed Coatings, *Thin Solid Films*, 1991, **200**, p 49-66.
52. J.D. Eshelby, The Elastic Field Outside an Ellipsoidal Inclusion, *Proc. R. Soc. A*, 1952, **252**, p 561-569.
53. Y. Okajima, T. Nakamura and S. Sampath, Effect of Powder Injection on the Interfacial Fracture Toughness of Plasma-Sprayed Zirconia, *J. Therm. Spray Technol.*, 2013, **22**, p 166-174.
54. R. Eriksson, H. Brodin, S. Johansson, L. Ostergren and X.H. Li, Fractographic and Microstructural Study of Isothermally and Cyclically Heat Treated Thermal Barrier Coatings, *Surf. Coat. Technol.*, 2014, **243**, p 82-90.
55. X. Zhang, M. Watanabe and S. Kuroda, Effects of Residual Stress on the Mechanical Properties of Plasma-Sprayed Thermal Barrier Coatings, *Eng. Fract. Mech.*, 2013, **110**, p 314-327.
56. M. Gizynski, X. Chen, N. Dusautoy, H. Araki, S. Kuroda, M. Watanabe and Z. Pakiela, Comparative Study of the Failure Mechanism of Atmospheric and Suspension Plasma Sprayed Thermal Barrier Coatings, *Surf. Coat. Technol.*, 2019, **370**, p 163-176.
57. Y. Zhao, L. Wang, J. Yang, D. Li, X. Zhong, H. Zhao, F. Shao and S. Tao, Thermal Aging Behavior of Axial Suspension Plasma-Sprayed Yttria-Stabilized Zirconia (YSZ) Thermal Barrier Coatings, *J. Therm. Spray Technol.*, 2014, **24**, p 338-347.
58. D. Zhou, J. Malzbender, Y.J. Sohn, O. Guillon and R. Vassen, Sintering Behavior of Columnar Thermal Barrier Coatings Deposited by Axial Suspension Plasma Spraying (SPS), *J Europ Ceram Soc*, 2019, **39**, p 482-490.
59. A. Bacciochini, J. Ilavsky, G. Montavon, A. Denoirjean, F. Benettouil, S. Valette, P. Fauchais and K. Wittman-Teneze, Quantification of Void Network Architectures of Suspension Plasma-Sprayed (SPS) Yttria-Stabilized Zirconia (YSZ) Coatings Using Ultra-Small-Angle X-ray Scattering (USAXS), *Mater. Sci. Eng. A*, 2010, **528**, p 91-102.

**Publisher's Note** Springer Nature remains neutral with regard to jurisdictional claims in published maps and institutional affiliations.